IEEE Access
Multidisciplinary | Rapid Review | Open Access Journal

Received 21 July 2022, accepted 31 July 2022, date of publication 5 August 2022, date of current version 18 August 2022.

Digital Object Identifier 10.1109/ACCESS.2022.3196774

RESEARCH ARTICLE

Scanning Path Planning of the Robot for Breast Ultrasound Examination Based on Binocular Vision and NURBS

XINRAN ZHANG[1], YONGDE ZHANG[1,2], (Member, IEEE), HAIYAN DU[1], MINGYUE LU[1], ZIXI ZHAO[1], YANHUA ZHANG[3], AND SIHAO ZUO[1,2]

[1]Key Laboratory of Advanced Manufacturing and Intelligent Technology, Harbin University of Science and Technology, Harbin 150080, China
[2]Foshan Baikang Robot Technology Company Ltd., Foshan 528237, China
[3]Department of Ultrasound, Harbin Medical University Cancer Hospital, Harbin 150080, China

Corresponding authors: Yongde Zhang (zhangyd@hrbust.edu.cn) and Yanhua Zhang (zhangyanhua09@126.com)

This work was supported in part by the Reserve Leader Funding Project of Leading Talent Echelon of Heilongjiang Province of China under Grant 2501050628, and in part by the Science and Technology Innovation Team Project of Foshan City of China under Grant 2018IT100302.

ABSTRACT Ultrasonic scanning is the most commonly used method for detecting breast cancer. Traditional breast ultrasound mainly relies on manual examination, which requires doctors with rich clinical experience. The scanning path planning of the robot for breast ultrasound examination based on binocular vision and non-uniform rational B-Splines (NURBS) is proposed in this paper to solve the limitations of traditional examination methods. First, breast images are acquired by the binocular camera. The depth information of the images is obtained through stereo matching, and the 3D point cloud reconstruction of the breast model is completed. Second, the spatial index algorithm based on the K-dimension tree (Kd-tree) and uniform sampling method are selected to denoise and down-sample the point cloud model to complete the preliminary optimization of the model. The point cloud information for the scanning path is extracted according to the method of point cloud extraction and the principle of normal vector calculation. Then, the interpolation optimization of the scanning path based on the NURBS curve is completed. The optimized scanning path is transformed into the robot motion path. Finally, the robot motion is simulated and analyzed, and the experimental results show that the rationality of robot operation and the smoothness of robot motion meet the requirements of path planning defined in this paper. The error analysis experiment shows that the path planned by this method can ensure the efficiency and accuracy of ultrasound examination.

INDEX TERMS Ultrasound examination, binocular vision, NURBS, scanning path planning, point cloud reconstruction, robot path planning.

I. INTRODUCTION

Breast cancer is a cancer with high morbidity and mortality worldwide. Its morbidity ranks first among female malignant tumors [1]. According to the 2020 cancer incidence statistics from the International Agency for Research on Cancer, there were approximately 2.3 million new cases of female breast cancer, accounting for 11.7% of new cases of cancer [2]. Early detection and timely treatment are the keys to curing breast cancer and increasing the survival rate [3], [4], [5]. Ultrasound examination is an important means to discover breast cancer [6], [7], [8]. However, ultrasound examination has higher requirements for the medical image analysis ability of doctors and is more dependent on clinical judgment experience. Different doctors often operate in different ways during ultrasound examination, which will lead to inconsistent diagnosis results. In addition, repetitive operations will cause serious fatigue damage to the doctor, and continuous probe pressure will aggravate the damage to the joint muscles of doctors [9]. The operation of ultrasonic scanning is relatively free. The examination process and operation are not standardized, resulting in inconsistent results. Robots can

The associate editor coordinating the review of this manuscript and approving it for publication was Yangmin Li.

assist doctors in completing breast ultrasound examinations, thus reducing the work intensity of doctors. Robots can accurately complete repetitive scanning operations to improve examination efficiency, standardize operation processes and reduce labor costs [10], [11], [12]. The robot for breast ultrasound examination requires high precision and efficiency to meet the scanning requirements. Therefore, it is very important to plan the scanning path of the robots [13], [14], [15]. The planned scanning path can more accurately detect the diseased position. In addition, doctors can pay more attention to ultrasonic diagnosis and treatment under the guidance of ultrasound images to ensure the operation effect.

In terms of robotic ultrasound examination, Abbasimoshaii *et al.* designed a new robot mechanism for ultrasonic imaging, and developed a new wiring mechanism to create the motion center for ultrasonic imaging [16]. Monfaredi *et al.* designed a new 6-DOF parallel robot [17]. The robot can be used to complete remote ultrasonic scanning operations. Sandoval *et al.* developed a new prismatic compliant joint (PCJ) coupled to the end-effector of cooperative robot for Doppler ultrasound examination [18]. Kojcev *et al.* compared the ultrasonic imaging of robots with that of expert system, and the results showed that the robotic ultrasound imaging can achieve more repeatable measurements [19]. Giuliani *et al.* proposed a user-centered method to develop a tele-operated robot for remote echocardiography [20]. The above systems have made beneficial progress for ultrasonic examination, but none of them has investigated the robot for breast ultrasound examination based on binocular vision and NURBS algorithm.

Traditional imaging systems use a single camera to generate two-dimensional images. The images lack necessary depth information. The systems rely too much on the experience of doctors, so the safety and stability of the operation cannot be guaranteed. Xu and Xia. designed a medical acupuncture robot for clinical treatment [21]. The robot mainly relies on real-time visual feedback from binocular camera when inserting needles. The automatic positioning of hundreds of acupuncture points requires the integration of robot and binocular camera. Lin *et al.* developed a 6-DOF prostate intervention serial robot, and established a binocular vision system (BVS) to evaluate the placement accuracy of the puncture needle and accurately locate the puncture point [22]. Zhang *et al*. designed a special binocular vision system, and put forward a tool center point (TCP) calibration method [23]. Xu *et al*. proposed an unsupervised learning method to reconstruct the accurate depth map for binocular 3D laparoscopy [24]. Wang *et al.* designed a new binocular vision registration method to develop a navigation robot based on CT images [25]. Jiang *et al.* studied the robot-assisted puncture process based on optical positioning technology [26]. Binocular camera is used for image acquisition in the system. All the above studies have made beneficial progress in the research of binocular vision in medical robots. Binocular vision can better obtain the depth data of relevant information. The breast model in the real scene is transformed into a 3D point cloud model in the visual interface.

NURBS curves are often used in robot path generation algorithms. Compared with other algorithms, the NURBS algorithm is more conducive to the generation and processing of multidimensional and irregular curves. Jahanpour *et al.* proposed a path planning method for parallel processing robots based on parametric NURBS curves [27]. Hashemian *et al.* proposed a reparameterization method of smooth trajectory curve based on jerk minimization, and introduced reparameterization function as unidirectional NURBS curve of the system time variable [28]. Wu *et al.* proposed a path planning method based on the NURBS curve with optimal robot performance [29]. By solving a multi-objective optimization problem, the optimal curve parameters and the execution time distributed along the curve segments can be obtained simultaneously. She and Tian. proposed a path control method for underwater robots based on NURBS curves [30]. These studies have promoted the application of the NURBS curve in robot path planning. NURBS algorithm makes the path smoother, and the curve fitting process does not deviate from the real line information. The NURBS algorithm can be used to better generate and optimize the scanning path of robots.

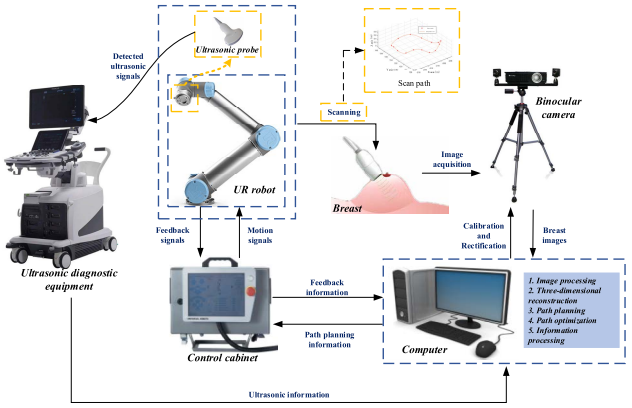

FIGURE 1. The complete robot system for breast ultrasound examination based on binocular vision.

In order to solve the above problems, the scanning path planning method of the robot for breast ultrasound examination based on NURBS and binocular vision is investigated. The complete ultrasonic scanning system is established, as shown in Figure 1. The depth information of the breast model is obtained by stereo matching with a binocular vision system, and then 3D point cloud reconstruction is carried out. The reconstructed 3D point cloud model of the breast is denoised and down-sampled. According to the optimized point cloud model, the normal vector is calculated, the ultrasonic scanning path is extracted by using normal vector information and spatial coordinate information, and the path is optimized and interpolated based on the NURBS curve. The optimized scanning path is transformed into the motion path of the robot, and the accuracy of the path planning result is proved by experiments.

II. THREE-DIMENSIONAL RECONSTRUCTION

A. BINOCULAR VISION CALIBRATION AND CORRECTION

The camera calibration can determine the internal relationship and transformation parameters among the world, camera and image pixels [31]. In the actual production process, the production, installation and other factors impact the accuracy of the camera, resulting in camera distortion. Therefore, the binocular camera should be calibrated [32].

A total of 30 shots were taken with binocular cameras for the calibration board with different angles. The position of the calibration board should be adjusted in the field of view of the binocular camera for each shot. The left-eye and right-eye cameras are calibrated separately, and the final rotation matrix R and translation vector T can be obtained through calculation. The calibration process is as follows:

1. The checkerboard calibration board is used. The calibration board consists of 8 × 6 squares, and the pixels of each square block are 25 mm × 25 mm.

2. The captured photos are imported into MATLAB calibration toolbox. The corner information of the photos obtained by the left and right cameras is extracted, as shown in Figure 2.

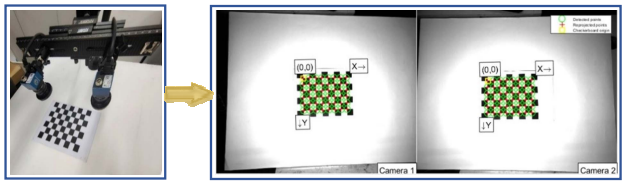

FIGURE 2. The corner information of left and right pictures.

3. The corner information is detected, and the calibration button is operated for calibration, so as to obtain the re-projection error information, as shown in Figure 3. The data with excessive re-projection error can be judged as singular values and deleted, and then the camera calibration can be performed again.

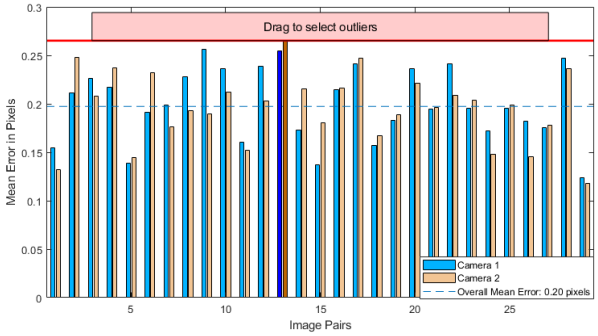

FIGURE 3. The re-projection error histogram of binocular camera.

4. The camera center calibration result diagram is obtained, as shown in Figure 4. The camera parameters can be exported from the workspace of the program operation results by clicking the Export button in the software operation interface.

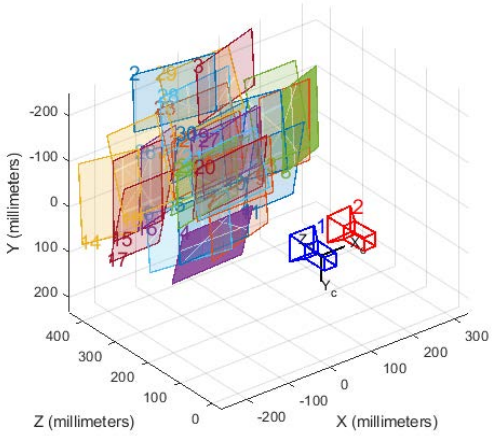

FIGURE 4. The camera center calibration result diagram.

TABLE 1. The camera calibration parameters.

Parameter type	Left camera parameter	Right camera parameter
Internal parameter	$\begin{bmatrix} 681.7239 & 0 & 0 \\ -0.1696 & 682.3153 & 0 \\ 647.3538 & 515.3412 & 1 \end{bmatrix}$	$\begin{bmatrix} 686.5444 & 0 & 0 \\ -0.1376 & 687.0185 & 0 \\ 650.0764 & 514.9415 & 1 \end{bmatrix}$
Radial distortion	$\begin{bmatrix} -0.0745 & 0.1404 & -0.0865 \end{bmatrix}$	$\begin{bmatrix} -0.0651 & 0.1146 & -0.0162 \end{bmatrix}$
Tangential distortion	$\begin{bmatrix} 5.3672\times10^{-4} & 8.4329\times10^{-4} \end{bmatrix}$	$\begin{bmatrix} 4.2624\times10^{-4} & 0.0010 \end{bmatrix}$

The calibration results are the parameters and distortion coefficients of binocular cameras. The camera distortion mainly comes from the radial and tangential direction, as shown in Equation (1). The internal parameter matrix, radial distortion parameter matrix and tangential distortion parameter matrix of the left and right cameras are shown in Table 1.

$$\begin{cases} \sigma_x(x,y) = x(k_1r^2 + k_2r^4 + k_3r^6 + \ldots) \\ \qquad + 2p_2xy + p_1(3x^2 + y^2) \\ \sigma_y(x,y) = y(k_1r^2 + k_2r^4 + k_3r^6 + \ldots) \\ \qquad + 2p_1xy + p_2(x^2 + 3y^2) \end{cases} \tag{1}$$

where (x, y) represents the actual coordinates in the case of distortion. $r^2 = x^2 + y^2$, K_i is the i-order radial deformation coefficient, and P_i is the i-order tangential deformation coefficient.

The external parameters of the left and right cameras are put into the same coordinate system to calculate the rotation parameters and translation parameters between the left and right cameras. The solution results of the binocular camera parameters are shown in Table 2.

The comparison before and after distortion correction is shown in Figure 5. Figure 5 shows that the corresponding points in the left and right images after distortion correction are on the same horizontal line.

TABLE 2. The binocular camera parameters.

Parameter type	Left camera parameter
Spin matrix R	$\begin{bmatrix} 0.9937 & 0.0057 & -0.0736 \\ -0.0069 & 0.9999 & -0.0149 \\ 0.0735 & 0.0154 & 0.9972 \end{bmatrix}$
Translation vector T	$\begin{bmatrix} -98.8979 & 4.0719 & -0.3026 \end{bmatrix}^T$

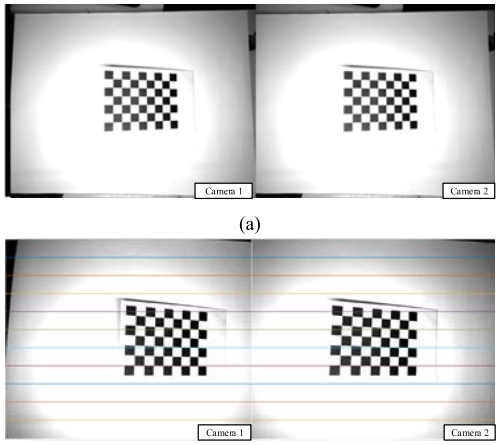

FIGURE 5. The distortion correction comparison experiment. (a) Before correction, (b) After correction.

B. STEREO MATCHING

Stereo matching is one of the important steps for obtaining a 3D point cloud model. Through stereo matching, the depth information can be obtained, thus obtaining the depth image.

1) MATCHING COST BASED ON CENSUS

For stereo matching, it is necessary to calculate the matching cost first. The purpose is to measure the similarity between the left and right image pixels. The smaller the matching cost, the better the similarity. The theoretical core of the census transformation method is to compare the gray values of the central pixel point P with those of the pixel point Q in its corresponding neighborhood. If the neighborhood pixel data in the gray value are larger than the center pixel data, the decision value is 0, otherwise it is 1. The value of bit strings is determined by the mapping relationship between them. The central pixel C_s is equal to the number of bit strings, as shown in Equation (2).

$$C_s(u, v) = \bigotimes_{i=-w}^{w} \bigotimes_{i=-h}^{h} \xi(I(u, v), I(u+i, v+j)) \tag{2}$$

where w and h represent half of the width and height of the window, respectively. C_s represents the census transform value of the center pixel. According to the census transformation value in Equation (2), the Hamming distance between the left and right images can be calculated.

$$C_s(u, v, d) = \text{Hammin g}(C_{sl}(u, v), C_{sr}(u-d, v)) \tag{3}$$

where $C_{sl}(u, v)$ is the pixel transformation value of left image, and $C_{sr}(u-d, v)$ is the pixel transformation value of right image.

2) COST AGGREGATION BASED ON PATH AGGREGATION

Because the calculation results are greatly affected by noise, the images should be filtered after cost matching. Therefore, through cost aggregation, the calculated matching cost can more accurately reflect the relevance between image pixels. Through the cost aggregation algorithm based on semi-global matching (SGM), the cost value under the path can be solved by aggregation on the path. The calculated total cost is the cost aggregation value. The calculation of the path cost of pixel p along path r is shown in Equation (4).

$$L_r(p, d) = C(p, d) + \min \begin{Bmatrix} L_r(p-r, d) \\ L_r(p-r, d-1) + P_1 \\ L_r(p-r, d+1) + P_1 \\ \min_i L_r(p-r, i) + P_2 \end{Bmatrix} - \min_i L_r(p-r, i) \tag{4}$$

where p is the pixel position and C(p, d) is the initial cost aggregation value.

The calculation equation of total path cost S is

$$S(p, d) = \sum_r L_r(p, d) \tag{5}$$

3) PARALLAX CALCULATION AND OPTIMIZATION

After cost aggregation, the calculation and optimization of image parallax should be completed on this basis. The winner takes all (WTA) algorithm is used to calculate parallax, and the calculation method is shown in Equation (6).

$$d_p = \arg\min_{d \in R_d} [C(p, d)] \tag{6}$$

where R_d is the allowable range of parallax and $C(p, d)$ is the matching cost of pixel p when the parallax is d.

The calculation result of parallax is optimized with the concept of minimum cost. The optimized result is taken as the optimal solution of the parallax calculation. In order to distinguish and remove the singular error value, it is necessary to judge the consistency between the left and right image lines of the parallax image after the parallax calculation, as shown in Equation (7).

$$D_p = \begin{cases} D_{bp} & \text{if } |D_{bp} - D_{mq}| \le 1 \\ D_{inv} & \text{otherwise} \end{cases} \tag{7}$$

where D_{bp} and D_{mq} are the disparity values corresponding to the pixels in the left and right images and D_{inv} is an invalid value.

The parallax algorithm based on the SGM is combined with the quadric interpolation process to improve the calculation precision. The quadratic curve can be fitted to approximate the optimal parallax result and the generation value on both sides. The algorithm also uses median filtering to suppress noise and ensure the edge accuracy. The disparity map of the breast model is shown in Figure 6.

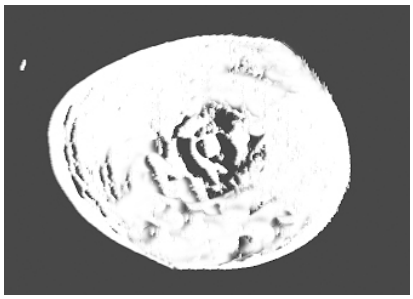

FIGURE 6. The disparity map of breast model.

C. RECONSTRUCTION OF 3D POINT CLOUD MODEL

According to the disparity map, the coordinate information corresponding to each pixel in the images can be calculated. The method based on spatial points is beneficial to realize rapid 3D point cloud reconstruction of breast model [33]. In the world coordinate system, there is a point P, and its corresponding spatial information is (X_w, Y_w, Z_w). p_1 and p_2 are the projection points of the coordinate points P on the left and right images. The corresponding coordinate information is $p_1(u_1, v_1)$ and $p_2(u_2, v_2)$, respectively.

$$Z_{cl}\begin{bmatrix} u_1 \\ v_1 \\ 1 \end{bmatrix} = \begin{bmatrix} m^1_{11} & m^1_{12} & m^1_{13} & m^1_{14} \\ m^1_{21} & m^1_{22} & m^1_{23} & m^1_{24} \\ m^1_{31} & m^1_{32} & m^1_{33} & m^1_{34} \end{bmatrix}\begin{bmatrix} X_w \\ Y_w \\ Z_w \\ 1 \end{bmatrix} \tag{8}$$

$$Z_{cr}\begin{bmatrix} u_2 \\ v_2 \\ 1 \end{bmatrix} = \begin{bmatrix} m^2_{11} & m^2_{12} & m^2_{13} & m^2_{14} \\ m^2_{21} & m^2_{22} & m^2_{23} & m^2_{24} \\ m^2_{31} & m^2_{32} & m^2_{33} & m^2_{34} \end{bmatrix}\begin{bmatrix} X_w \\ Y_w \\ Z_w \\ 1 \end{bmatrix} \tag{9}$$

where $(u_1, v_1, 1)$ and $(u_2, v_2, 1)$ represent the homogeneous coordinates of the left and right imaging points p_1 and p_2 of point P, respectively. $(X_w, Y_w, Z_w, 1)$ represents the homogeneous coordinate of space point P. Z_{cl} and Z_{cr} are the z coordinate values in the left and right coordinate systems. m^i_{ab} represents the element in row a and column b of the perspective projection matrix M^i.

The matrix equation (10) is obtained by deducing Equation (8) and (9).

$$\begin{bmatrix} (u_1m^1_{31} - m^1_{11}) & (u_1m^1_{32} - m^1_{12}) & (u_1m^1_{33} - m^1_{13}) \\ (v_1m^1_{31} - m^1_{21}) & (v_1m^1_{32} - m^1_{22}) & (v_1m^1_{33} - m^1_{23}) \\ (u_2m^2_{31} - m^2_{11}) & (u_2m^2_{32} - m^2_{12}) & (u_2m^2_{33} - m^2_{13}) \\ (v_2m^2_{31} - m^2_{21}) & (v_2m^2_{32} - m^2_{22}) & (v_2m^2_{33} - m^2_{23}) \end{bmatrix} \times \begin{bmatrix} X_w \\ Y_w \\ Z_w \end{bmatrix} = \begin{bmatrix} m^1_{14} - u_1m^1_{34} \\ m^1_{24} - v_1m^1_{34} \\ m^2_{14} - u_2m^2_{34} \\ m^2_{24} - v_2m^2_{34} \end{bmatrix} \tag{10}$$

Equation (10) is further simplified to obtain Equation (11).

$$AX = B \tag{11}$$

The three-dimensional coordinates of space point P in the world coordinate system are obtained by solving the pseudo inverse of matrix A. According to the calculated 3D coordinates, the point cloud data can be reconstructed, as shown in Figure 7.

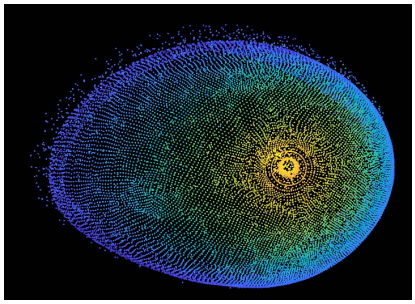

FIGURE 7. The 3D point cloud image of breast model.

III. PATH EXTRACTION

A. POINT CLOUD DENOISING

There are a lot of noise points in the point cloud model obtained by the 3D reconstruction. If all the point cloud data are directly used to plan the scanning path, it will not only have redundant information, but also seriously affect the real-time performance of the system. It is necessary to denoise the reconstructed point cloud model to extract the path points more accurately. The Kd-tree spatial index algorithm is used to filter and denoise point clouds. For any point p_i in point cloud $p = \{p_i, i = 1, 2, 3 \ldots, p_i \in R^3\}$, the k neighborhood search method can be used. The set of selected points in the k neighborhood is denoted as $p_{ij} = \{p_{i1}, p_{i2}, p_{i3}, p_{i4}, \ldots, p_{ik}\}$. According to the average distance from point p_i to the neighboring points, the point cloud noise is removed, as shown in Equation (12).

$$p^* = \left\{ p_i^* \in P \left| (\mu_N - \alpha\sigma_N) \le \overline{d_i}^* \le (\mu_N + \alpha\sigma_N) \right. \right\} \tag{12}$$

where $\overline{d_i}^*$ is the average distance from point p_i to all points in the k neighborhood. α is the adjustment factor of the control threshold. μ_N is the average distance of the whole point cloud. σ_N is the standard deviation of the distance of the whole point cloud. If the relationship between $\overline{d_i}^*$ and $\mu_N \pm \alpha\sigma_N$ meets the requirements of Equation (12), the points will be reserved, otherwise, the points will be removed. The denoising process of Kd-tree algorithm is shown in Figure 8.

When $k = 10, 15, 20$, the denoising effect of the breast model is shown in Figure 9. The denoising process is carried out on the point cloud models with k values ranging from 2 to 20. The experimental data of denoising of the point cloud model are shown in Figure 10.

The results show that the calculation time is prolonged with the increase of k value. The number of point clouds increases with the increase of k value, and it is in a stable state after reaching a certain value. Considering the experimental results and filtering effect, $k = 15$ is used for filtering.

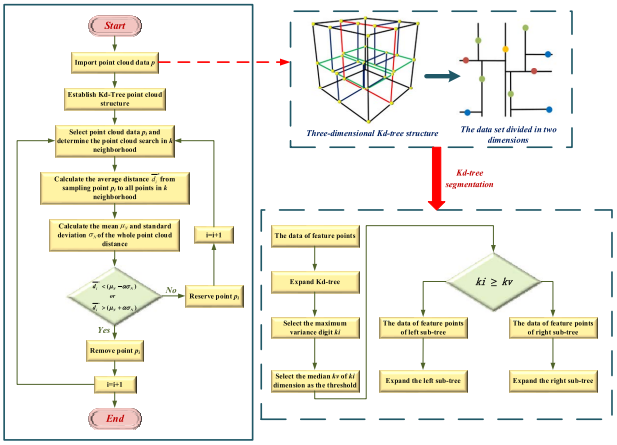

FIGURE 8. The flow chart of Kd-tree point cloud denoising.

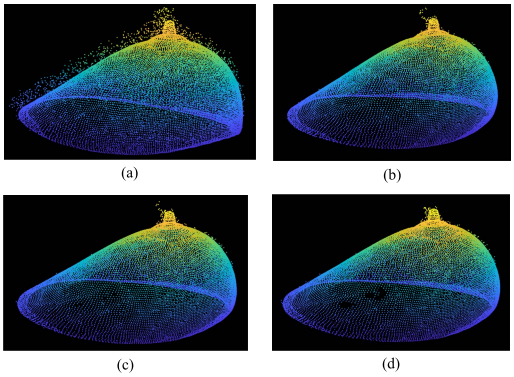

FIGURE 9. The effect diagram of breast model denoising with different k values. (a) The original point cloud image, (b) $k = 10$, (c) $k = 15$, (d) $k = 20$.

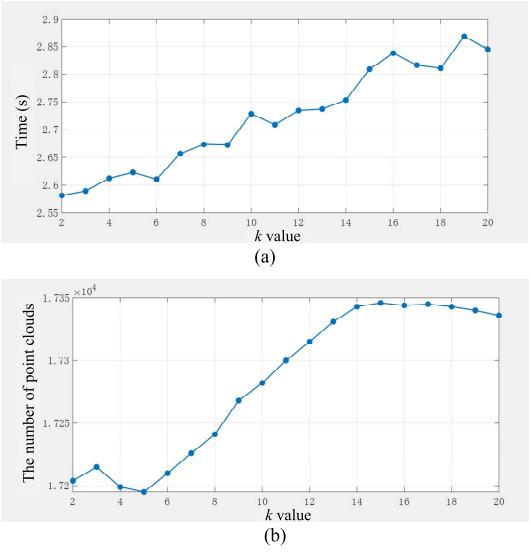

FIGURE 10. The experimental data of denoising of point cloud model. (a) The diagram of k value and time, (b) The Graph of k value and number of point clouds.

B. DOWN-SAMPLING

Down-sampling refers to reducing the number of point clouds while ensuring that the geometric structure of point clouds does not change. Because the number of point clouds after filtering and denoising is still large, the subsequent path extraction and other related processing are time-consuming, which affects the real-time performance of the system. Therefore, it is necessary to perform down-sampling processing to improve the computational efficiency. The commonly used down-sampling methods include grid sampling, uniform sampling and geometric sampling. The comparison diagram of point cloud models obtained by several point cloud down-sampling algorithms is shown in Figure 11. The comparison of the several methods is shown in Table 3. When dealing with the point cloud model by grid sampling, the number of sampling points in each grid cannot be accurately controlled, which will lead to uneven distribution of point clouds. To keep the point cloud evenly distributed, smaller grid points need to be used for down-sampling. However, this method will make the sampling effect unobvious and time-consuming. When the point cloud model is processed by geometric down-sampling, the distribution density of the point cloud changes with the curvature, which leads to the uneven distribution of point clouds.

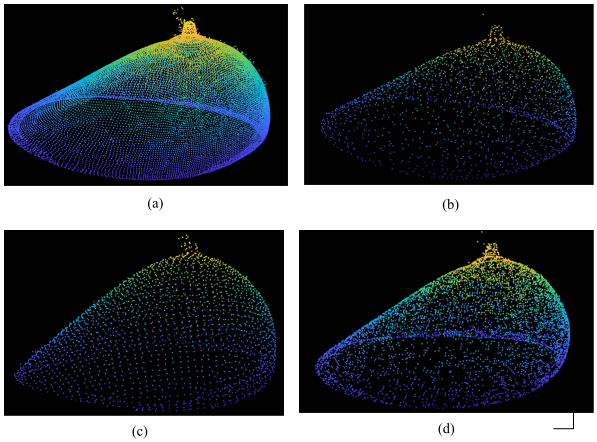

FIGURE 11. The comparison diagram of point cloud models obtained by several point cloud down-sampling algorithms. (a) The original point cloud image, (b) Grid sampling, (c) Uniform sampling, (d) Geometric sampling.

It can be seen from Figure 11 and Table 3 that uniform sampling should be selected for the down-sampling. The obtained point cloud data are uniformly distributed, which is convenient for subsequent path extraction and planning.

C. NORMAL VECTOR CALCULATION

Generally, doctors need to ensure that the ultrasonic probe keeps vertical contact with the skin surface. The normal vector of the breast surface can determine the pose of the ultrasound probe. The normal vectors of point clouds are calculated by the method based on local surface data fitting to reduce the calculation time. According to the point cloud data in a certain range near the calculated point, the surface normal vectors are calculated. The method has good real-time performance and ensures the processing speed and accuracy,

TABLE 3. The sampling characteristics under point cloud.

Down-sampling type	Advantage	Disadvantage
Grid sampling	➢ High sampling efficiency; ➢ Uniform sampling distribution points; ➢ Controllable spacing between points.	➢ The number of sampling points cannot be accurately controlled.
Uniform sampling	➢ Uniform distribution of sampling points; ➢ Sampling points are preferentially distributed on the edges; ➢ Geometric edges can be preserved.	➢ The algorithm complexity is high; ➢ Repeated calculations are frequent; ➢ Low efficiency.
Geometric sampling	➢ High calculation efficiency; ➢ The distribution of sampling points in local area is highly uniform.	➢ The number distribution of point clouds changes with the change of geometric characteristics; ➢ Low overall uniformity.

as shown in Equation (13).

$$\begin{bmatrix} \sum_{i=1}^{k} x_i^2 & \sum_{i=1}^{k} x_i y_i & \sum_{i=1}^{k} x_i z_i \\ \sum_{i=1}^{k} x_i y_i & \sum_{i=1}^{k} y_i^2 & \sum_{i=1}^{k} y_i z_i \\ \sum_{i=1}^{k} x_i z_i & \sum_{i=1}^{k} y_i z_i & \sum_{i=1}^{k} z_i^2 \end{bmatrix} \begin{bmatrix} a \\ b \\ c \end{bmatrix} = \gamma \begin{bmatrix} a \\ b \\ c \end{bmatrix} \tag{13}$$

Equation (13) can be simplified to Equation (14).

$$Ax = \gamma x \tag{14}$$

According to the eigenvalue solution and eigenvector analysis of matrix A, the normal vector of this point is equivalent to the eigenvector of the minimum eigenvalue of the covariance matrix. The problem of uncertainty of normal direction can be solved by completing the operation of the unified direction. The unified optimization is carried out by using the line-of-sight direction characteristic, as shown in Equation (15). The calculation result of the normal vector of the breast model is shown in Figure 12.

$$\begin{cases} \overrightarrow{v} = (-x, -y, -z)^T \\ \overrightarrow{v} \cdot \overrightarrow{n} > 0 \end{cases} \tag{15}$$

D. PATH EXTRACTION METHOD

According to the reconstructed 3D breast model, the extraction method of the scanning path is obtained.

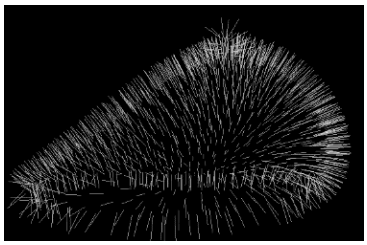

FIGURE 12. The calculation results of normal vector of breast model.

1. The selected point cloud data can form a closed loop on the X-Y projection plane. The point cloud data should be outside or on the surface of the breast. The number of point clouds should be properly selected. The coverage of the point cloud should be reasonable, not too close to the top or bottom of the breast. The extracted point cloud data should be prevented from being distributed in a larger range in the z-axis.

2. The 3D point cloud model was imported into MATLAB. Then, the coordinate information of each point cloud under the rectangular coordinate system is calculated, as shown in Figure 13.

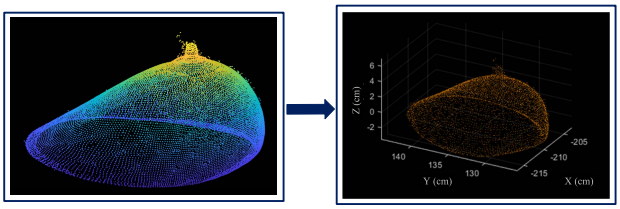

FIGURE 13. The point cloud distribution map of breast model in cartesian coordinate system.

3. Half of the height of the breast in the z-axis is selected as the plane of the scanning path. All coordinate information of the 3D point cloud model in the z-axis is derived. The z-axis median of the point cloud model is the average of the z-axis maximum and the z-axis minimum. A suitable scanning range can be obtained in this way. Moreover, the scanning path can form a closed loop on the X-Y projection plane in the subsequent processing. The formed point cloud data are conducive to smooth processing.

4. The scanning path is extracted in MATLAB according to the median value of the z-axis. The normal vector information is generated in the extracted 3D point cloud model, as shown in Figure 14.

IV. PATH PLANNING BASED ON NURBS CURVE

The NURBS curve is an improved non-uniform rational B-spline curve based on B-spline curve. Its core improvement lies in adding the weight factors corresponding to the control points, so that the fitting and smoothing process of the polyline does not deviate from the real line information [34].

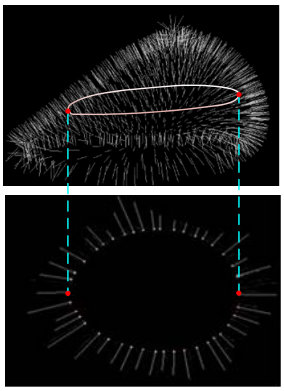

FIGURE 14. The normal vector of breast ultrasound examination path.

A. GENERATION OF NURBS CURVES

The equation for NURBS curve is

$$p(u) = \frac{\sum_{i=0}^{n} \omega_i d_i N_{i,k}(u)}{\sum_{i=0}^{n} \omega_i N_{i,k}(u)} \tag{16}$$

Among them,

$$\begin{cases} N_{i,0} = \begin{cases} 1 & u \in [u_i, u_{i+1}] \\ 0 & other \end{cases} \\ N_{i,k}(u) = \dfrac{u - u_i}{u_{i+k+1} - u} N_{i,k-1}(u) \\ \qquad + \dfrac{u_{i+k} - u}{u_{i+k} - u_{i+1}} N_{i+1,k-1}(u) \\ \dfrac{0}{0} = 0 \end{cases} \tag{17}$$

The recursive method in Equation (17) mainly deduces the method of directly solving $N_{i,k}(u)$. Using the direct solution, the solution of any point needs to be recurred $(n+1)(2^k-1)$ times. This method will make it necessary to calculate the coordinate value of any point on the NURBS curve, which is unfavorable to the real-time performance of the whole system. However, the De Boer recursive method only needs to convert the calculated high-dimensional coordinate value into the low-dimensional spatial coordinate value through the central projection. The algorithm can avoid a large number of calculations. The recursive equation is (18), as shown at the bottom of the page.

In Equation (18), ω_i is the weight factor corresponding to the control vertex $d_i (i = 0, 1, \ldots\ldots, n)$. The k-th B-spline basis function $N_{i,k}(u)$ can be calculated by the node vector $u = [u_0, u_1, \ldots\ldots, u_{n+k+1}]$. i is the serial number, and k is the spline order. The NURBS curve is an open curve, and has the characteristic of an unclosed data link. The repeatability of nodes at both ends is set as $r = k + 1$ in the adjustment process. The generation of curves is determined by the calculation of node vectors, the determination of boundary conditions and the inverse calculation of corresponding control vertices.

The cumulative chord length parameterization algorithm is the commonly used algorithm to calculate and determine node vectors. The accumulated chord length parameter method can faithfully show the distribution of data points without being limited by chord length. Moreover, the interpolation curve of the cumulative chord parameter method has good smoothness, which can reflect the curve shape of data points more accurately and truly. The specific parameterization method of cumulative chord length is as follows.

$$\begin{cases} u_0 = u_1 = u_2 = u_3 = 0 \\ u_{n+3} = u_{n+4} = u_{n+5} = u_{n+6} = 1 \\ \qquad i = 1, 2, \ldots\ldots, n-1 \\ u_{i+3} = i/n \end{cases} \tag{19}$$

Then the boundary conditions of the curve are determined. The tangent vector condition is used to calculate the position of the control points. The tangential direction of the first and last breakpoint should be fixed. The tangent vector condition is

$$\begin{cases} d_1 - d_0 = \dfrac{\Delta_3}{3} p_0' \\ d_{n+2} - d_{n+1} = \dfrac{\Delta_{n+2}}{3} p_n' \end{cases} \tag{20}$$

where $\Delta_i = u_{i+1} - u_i$. p_0' and p_n' are the tangent vectors of the head and end point. The repetition degree of the end point of the cubic NURBS curve is set to 4. The control points at both ends of the curve are equivalent to the data points, that is, $d_0 = P_0$, $d_{n+2} = P_n$. Because the extracted path is a closed curve, the data points are closed. Therefore, $n + 1$ control vertices can be obtained by $n - 1$ equations. The inverse calculation

$$\begin{cases} q(u) = \sum_{j=i-k}^{i-l} d_j^l N_{j,k-l}(u) = \ldots = d_{i-k}^k, \quad u \in [u_i, i_{i+1}] \subset [u_k, u_{n+1}] \\ d_j^l = \begin{cases} d_j, & l = 0 \\ (1-\alpha_j^l) d_j^{l-1} + \alpha_j^l d_{j+1}^{l-1}, & j = i-k, \ldots, i-1, \quad l = 1, 2 \ldots, k \end{cases} \\ \alpha_j^l = \dfrac{u - u_{j+l}}{u_{j+k+1} - u_{j+l}}, \qquad \dfrac{0}{0} = 0 \end{cases} \tag{18}$$

result of the control vertices of the cubic curve is as follows.

$$\begin{bmatrix} 1 & & & & & & \\ a_2 & b_2 & c_2 & & & & \\ & \cdot & \cdot & \cdot & & & \\ & & \cdot & \cdot & \cdot & & \\ & & & \cdot & \cdot & \cdot & \\ & & & & a_n & b_n & c_n \\ & & & & & & 1 \end{bmatrix} \begin{bmatrix} d_1 \\ d_2 \\ \cdot \\ \cdot \\ \cdot \\ d_n \\ d_{n+1} \end{bmatrix} = \begin{bmatrix} e_1 \\ e_2 \\ \cdot \\ \cdot \\ \cdot \\ e_n \\ e_{n+1} \end{bmatrix} \tag{21}$$

where d_i is the control vertex. $\Delta_i = u_{i+1} - u_i (i = 0, 1, 2, \ldots, n)$. The meaning of each parameter in Equation (21) is

$$\begin{cases} a_i = \dfrac{(\Delta_{i+2})^2}{\Delta_i + \Delta_{i+1} + \Delta_{i+2}} \\ b_i = \dfrac{\Delta_{i+2}(\Delta_i + \Delta_{i+1})}{\Delta_i + \Delta_{i+1} + \Delta_{i+2}} + \dfrac{\Delta_{i+1}(\Delta_{i+2} + \Delta_{i+3})}{\Delta_{i+1} + \Delta_{i+2} + \Delta_{i+3}} \\ c_i = \dfrac{(\Delta_{i+1})^2}{\Delta_{i+1} + \Delta_{i+2} + \Delta_{i+3}} \\ e_i = p_0 - \dfrac{\Delta_3}{3} p_0' \\ e_{n+1} = p_n - \dfrac{\Delta_{n+2}}{3} p_n' \\ e_i = (\Delta_{i+1} + \Delta_{i+2}) p_{i-1} \end{cases} \tag{22}$$

where $\Delta_i = u_{i+1} - u_i$, $i = 1, 2, \ldots, n$. All control vertex values can be obtained by solving Equation (22).

B. NURBS CURVE INTERPOLATION

NURBS curve interpolation is one of the important steps in path planning. Its main function is to calculate the movement distance required for each interpolation cycle according to the given movement speed. Part of the coordinate values on the motion path are calculated as interpolation values. The realization process optimizes and fits the chord length of two adjacent interpolation points into the actual curve [35]. During the interpolation process, it is necessary to segment curves quickly and calculate the coordinate values of interpolation points accurately.

The principle of the NURBS interpolation algorithm is to solve the interpolation coordinate point $\{C(u_0), C(u_1), \ldots, C(u_{n-1}), C(u_n)\}$ based on time series $\{t_0, t_1, \ldots, t_{n-1}, t_n\}$ and corresponding parameters $\{u_0, u_1, \ldots, u_{n-1}, u_n\}$. The interpolation point $C(u_i)$ and its corresponding parameter u_i, the interpolation point $C(u_{i+1})$ and its corresponding parameter u_{i+1} are known. The curve length between two interpolation points is ΔS_i, and the actual feed length is the chord length ΔL_i. The calculation method is

$$\Delta L_i = V(u_i) T_s = \|C(u_{i+1}) - C(u_i)\| \tag{23}$$

where T_s is the interpolation cycle and $V(u_i)$ is the current feed speed. The direction of the current feed speed $V(u_i)$ is the direction of movement along the chord length ΔL_i. The direction of the actual moving speed should be along the direction of curve ΔS_i. There will be corresponding errors when calculating the parameters of the next interpolation point. The errors will lead to a certain deviation between the actual value and the expected value of the next interpolation point u_{i+1}. The actual feed speed is expressed by Equation (24).

$$V_r(u_i) = \frac{\Delta L_i}{T_s} = \frac{\|C(u_{i+1}) - C(u_i)\|}{T_s} \tag{24}$$

There is an inherent error between the actual feed speed and the desired feed speed. The error will lead to velocity fluctuation, and the fluctuation degree is described by using the speed fluctuation ratio δ, as shown in Equation (25).

$$\begin{aligned} \delta_i &= \frac{V_r(u_i) - V(u_i)}{V(u_i)} \times 100\% \\ &= \frac{\|C(u_{i+1}) - C(u_i)\| - V(u_i) T_s}{V(u_i) T_s} \times 100\% \end{aligned} \tag{25}$$

Excessive speed fluctuation will make the robot shake greatly in the process of motion, which will lead to the decrease of system stability. Therefore, the speed fluctuation should be restrained at all times in the interpolation process. The interpolation accuracy of the NURBS curve is often described by the chord error. The chord error is the maximum difference between chord length and actual curve in the interpolation period. The smaller the chord error, the closer the chord length is to the actual curve. The smaller the velocity fluctuation ratio is, the more stable the ultrasound examination is.

The arc approximation method is used to calculate the chord error. The curve segment is approximately equivalent to the arc. The arc height error is the distance between the arc and chord length. The curvature will influence the chord error. The chord length ΔL_i is related to the feed speed. Therefore, the feed speed will be limited by the curvature and chord error. If the maximum allowable chord error h_{max} is introduced as the error control standard, the feed speed at the parameter u_i of any interpolation point is

$$V_c(u_i) = \frac{2}{T_s} \sqrt{\rho_i^2 - (\rho_i - h_{max})^2} \tag{26}$$

where ρ is the curvature of the approximate arc.

In the process of interpolation, different curvatures will produce different centrifugal forces. The centrifugal force will partially affect the accuracy of ultrasonic examination. The centrifugal force can be controlled by controlling the normal acceleration. The limitation value of the feed speed can be expressed as

$$V(u_i) = \min \left\{ \frac{2}{T_s} \sqrt{\rho_i^2 - (\rho_i - h_{max})^2}, \sqrt{\rho_i A_{n,max}}, V_{max} \right\} \tag{27}$$

where $A_{n,i}$ is the normal acceleration and $A_{n,max}$ is the maximum normal acceleration. Equation (27) shows that the limit of the feed speed is mainly related to the maximum chord error, curve curvature, normal acceleration and maximum allowable speed of the system.

The second-order Taylor expansion is used to determine the relationship between the interpolation time t and corresponding parameter u, denoted by $u(t_i) = u_i$ and $u(t_{i+1}) = u_{i+1}$. The relationship between interpolation time and corresponding parameters can be converted into the relationship between u_i and u_{i+1}. The Taylor expansion equation of u at time t_i is

$$u(t) = u(t_i) + u(t)(t - t_i) + \frac{u''(t)}{2!}(t - t_i)^2 + O((t - t_i)^3) \tag{28}$$

The relationship between parameters u_i and u_{i+1} is shown in Equation (29).

$$u_{i+1} = u_i + \frac{V(u)T_s}{\|C'(u)\|} - \frac{V^2(u)T_s^2[C'(u) - C''(u)]}{2\|C'(u)\|^2} \tag{29}$$

where $C'(u)$ and $C''(u)$ are the first and second derivatives of the curve, respectively. The calculation process can be expressed as (30) and (31), shown at the bottom of the page.

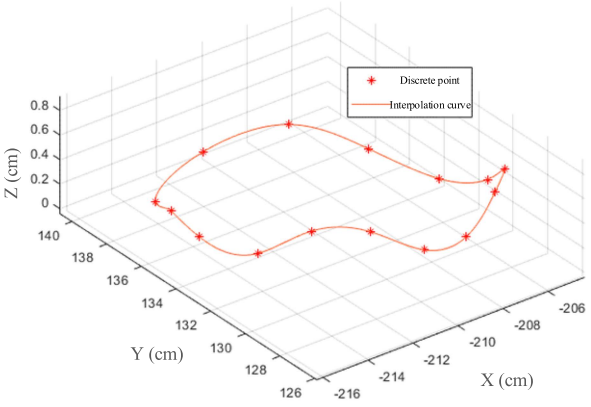

FIGURE 15. The schematic diagram of the robot motion path after interpolation.

The extracted path points are interpolated and optimized by NURBS curves. The interpolation results are shown in Figure 15.

V. EXPERIMENTS AND RESULTS

A. HAND-EYE CALIBRATION EXPERIMENT

Through the hand-eye calibration experiment, the coordinate relation between the binocular camera and robot can be established. The calibration experiment was carried out according to the requirements of breast ultrasound examination, as shown in Figure 16(a). The robot should be moved at least twice to calculate the results of hand-eye calibration data, as shown in Figure 16(b). The spatial position information between the binocular camera base and the robot base is relatively fixed. The matrix A represents the spatial position of the end-effector in the coordinate system of the robot base. The spatial position of the calibration plate in the robot end coordinate system can be expressed by matrix B. The matrix C represents the spatial position of the camera in the calibration plate coordinate system, that is, the external parameters of the camera. The matrix D represents the spatial position of the camera in the coordinate system of the robot base, that is, the parameters to be solved for hand-eye calibration. Moreover, it is necessary to ensure that both positions can make the calibration plate within the shooting range of the binocular camera. The hand-eye calibration process is shown in Figure 17.

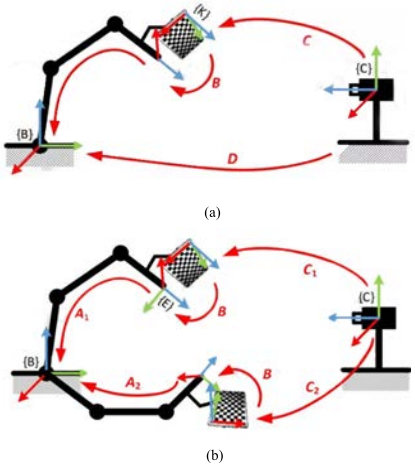

FIGURE 16. The schematic diagram of single and multiple hand-eye calibration. (a) The schematic diagram of hand-eye calibration system, (b) The schematic diagram of multiple hand-eye calibration.

The chessboard calibration board is installed at the end of the robot. The coordinate information of the vertices of the calibration board relative to the coordinate system of the robot base under different robot postures is calculated. According to the internal and external parameters of distortion correction, the spatial information of the vertices in

$$C'(u) = \frac{\sum_{i=0}^{n} \omega_i d_i N'_{i,k}(u) - C(u) \sum_{i=0}^{n} \omega_i N'_{i,k}(u)}{\sum_{i=0}^{n} \omega_i N_{i,k}(u)} \tag{30}$$

$$C''(u) = \frac{\sum_{i=0}^{n} \omega_i d_i N''_{i,k}(u) - 2C'(u) \sum_{i=0}^{n} \omega_i N'_{i,k}(u) - C(u) \sum_{i=0}^{n} \omega_i N''_{i,k}(u)}{\sum_{i=0}^{n} \omega_i N_{i,k}(u)} \tag{31}$$

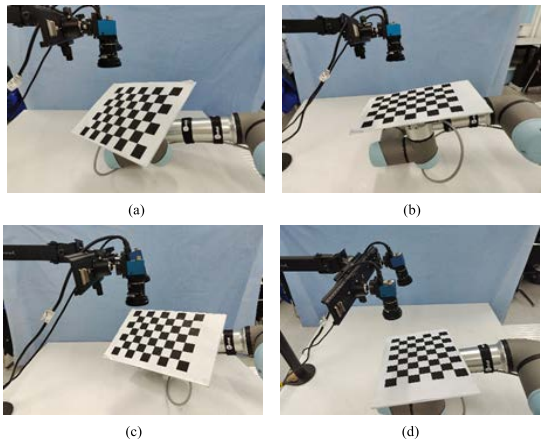

FIGURE 17. The hand-eye calibration experiment. (a) Position 1, (b) Position 2, (c) Position 3, (d) Position 4.

the camera coordinate system is solved. Through multiple measurements, the spatial coordinate data of the vertices are obtained. Using the obtained data, the transformation matrix between the robot and binocular camera can be obtained, as shown in Equation (32).

$$B = \begin{pmatrix} 0.972 & 0 & 0 & 0.152 \\ 0 & 0.965 & -0.196 & 0.003 \\ 0 & 0.196 & 0.965 & -0.540 \\ 0 & 0 & 0 & 1 \end{pmatrix} \quad (32)$$

B. ROBOT PATH PLANNING EXPERIMENT

1) SIMULATION EXPERIMENT OF MOTION PATH

Fifteen point cloud coordinates are chosen to represent the obtained ultrasonic scanning path. The fifteen point cloud coordinates are connected end to end with a closed curve as the initial movement path of the robot in MATLAB. NURBS curves are used to optimize the path. The optimized motion path is shown in Figure 18. It can be known from Figure 18 that a smoother path curve can be obtained by extracting the ultrasonic scanning path points with NURBS curve interpolation.

Before the actual operation, it is necessary to set the motion parameters of the robot and analyze the speed parameters, so as to verify the rationality and compliance of the robot movement under the set path planning. The UR5e robot model is imported into Vrep. After adding Dummy tracking points, the inverse kinematics are solved. Then, the smoothed path and human model are imported into Vrep. The path is presented in the form of a three-dimensional closed curve. The positional relationship among the path, breast model and robot is set, as shown in Figure 19(a). The motion speed and acceleration of the robot are set to 0.025 m/s and 0.02 m/s^2 respectively in the path execution code. The graph grab points are added to each joint of the robot. When the robot joint moves, it can track and acquire the motion information. The changes of the joint angle and joint angular velocity are shown in Figure 19(b) and Figure 19(c). The postures of the calculated motion path points all meet the range of joint motion. The joint changes continuously and steadily, and there is no sudden change of the joint angle. The peak value is the result of joint 6 swinging back and forth when the robot moves along the path, as shown in Figure 19(c). During the movement of the robot, the rotation and swing amplitude of joint 6 are large. Although the peak value appears, the speed of joint 6 does not exceed the speed constraint limit.

The simulation results show that the speed parameters are set properly and the robot motion is smooth. The acceleration setting enables the robot to have sufficient real-time response capability. The motion effect of the robot is consistent with the path planning scheme. The robot can complete the scheduled operation in a reasonable way.

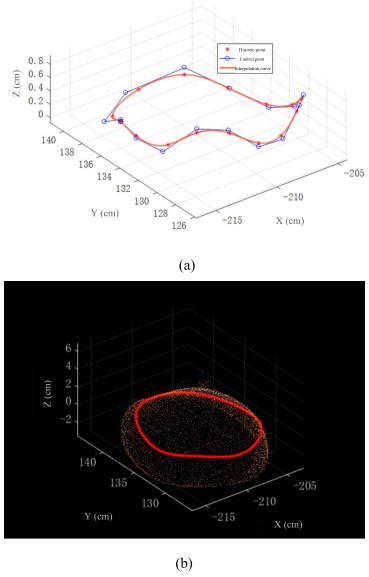

FIGURE 18. The results of motion path planning. (a) The comparison diagram of path curves before and after interpolation, (b) The path model diagram after interpolation.

2) ERROR ANALYSIS EXPERIMENT

After completing the above experiments, the experimental platform of breast ultrasound examination based on the UR5e robot is built, as shown in Figure 20. The platform is composed of UR5e robot and controller, 3D printed breast model, computer, ultrasonic probe (C1-7/60R) and binocular vision system (two CMOS cameras, DFK 33UP1300, 1.3 million pixels, 95fps).

The breast model photos obtained by the binocular camera are sent to the computer. The computer reconstructs the three-dimensional point cloud model, processes the point cloud data, and extracts the ultrasonic scanning path. Then, the NURBS curve is used to optimize the ultrasonic scanning path and plan the motion path of the robot. Finally, the relevant control instructions are transmitted to the control cabinet through the Ethernet, so as to control the robot to complete the operation of breast ultrasound examination. The path coordinate information and errors are obtained through the actual experiment, as shown in Table 4.

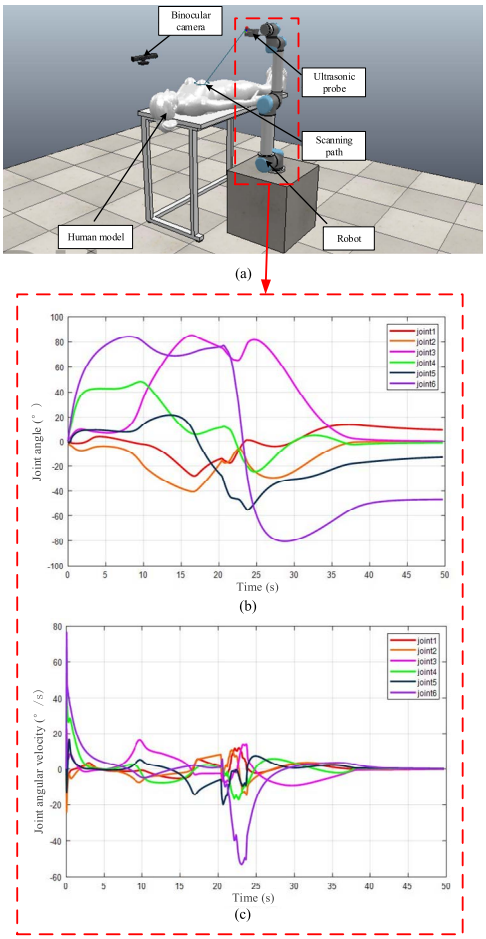

FIGURE 19. The motion simulation of the robot for breast ultrasound examination. (a) The simulation scenario configuration, (b) The joint angle change graph, (c) The joint angular velocity change graph.

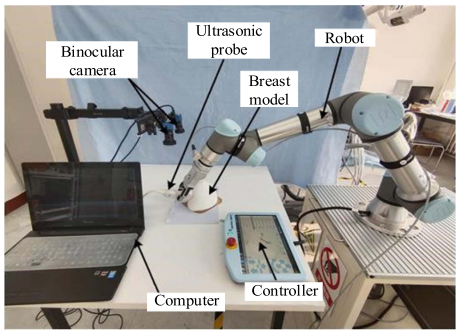

FIGURE 20. The robot experimental platform for breast ultrasound examination.

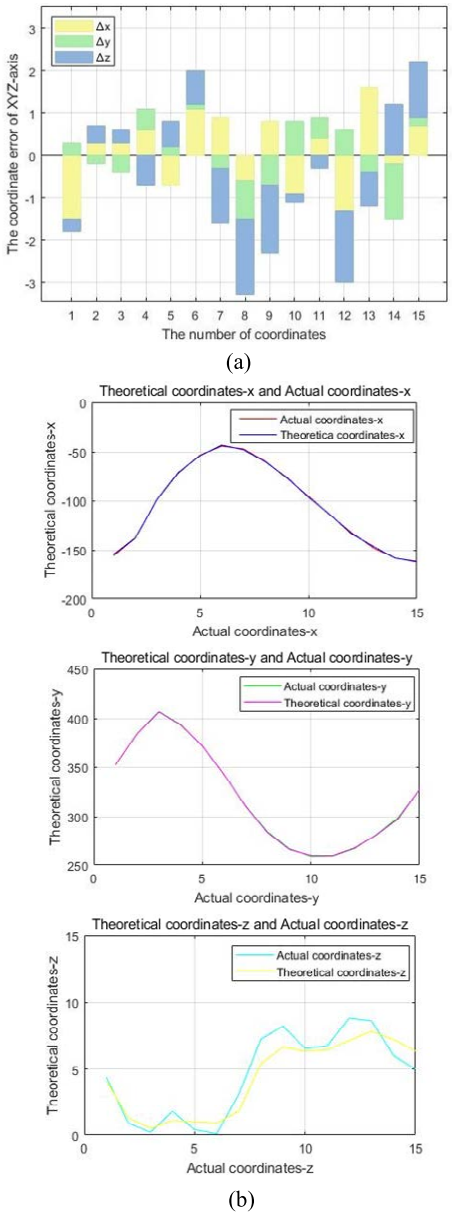

FIGURE 21. The coordinate error between the theoretical path and actual path in XYZ direction. (a) The histogram of coordinate error of XYZ-axis, (b) The error between theoretical coordinate and actual coordinate in XYZ-axis.

The theoretical path is the path generated by optimizing the path extracted from the 3D point cloud model by the interpolation algorithm. If only the 3D reconstruction model is used to determine the extracted scanning path, the rationality and smoothness of the scanning path cannot be guaranteed, and the scanning time and efficiency will also be affected. The NURBS curve algorithm is used to optimize the path interpolation to improve the scanning efficiency. The actual path is the actual movement path of the robot. In the process of ultrasonic scanning, the robot may have great jitter because of the speed fluctuation, which leads to the decrease of the system stability. It is easy to cause damage to the human body during ultrasonic examination. Therefore, the NURBS curve algorithm is used to improve the interpolation accuracy to suppress the speed fluctuation all the time, so that the robot can hold the ultrasonic probe more smoothly for detection. When the robot moves along the planned trajectory, the interactive force between the ultrasonic probe and the breast will be generated. The robot system for breast ultrasound examination needs the function of real-time force feedback. A six-dimensional force sensor is used to collect the contact force signal between the ultrasonic probe and tissue. The

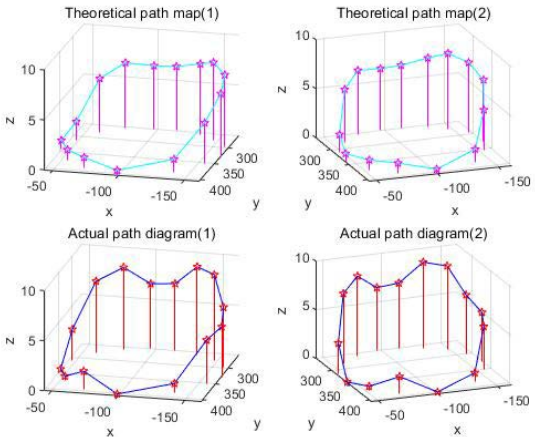

FIGURE 22. The path comparison between original coordinates and actual coordinates.

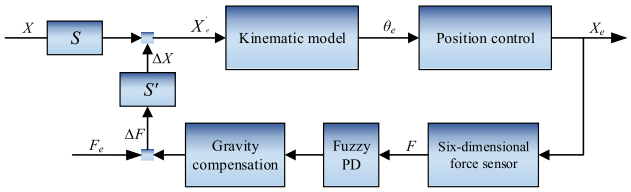

FIGURE 23. The structural block diagram of force feedback pose adjustment.

TABLE 4. The path coordinate information and error.

Path point	Theoretical coordinates /mm	Actual coordinates /mm	Error /mm		
	(x_0, y_0, z_0)	(x, y, z)	Δx	Δy	Δz
1	(-154.5, 352.3, 4.1)	(-156.0, 352.0, 4.4)	-1.5	0.3	-0.3
2	(-137.8, 384.1, 1.3)	(-138.1, 384.3, 0.9)	0.3	-0.2	0.4
3	(-99.2, 406.6, 0.5)	(-99.5, 407.0, 0.2)	0.3	-0.4	0.3
4	(-71.2, 393.3, 1.1)	(-71.8, 393.8, 1.8)	0.6	0.5	-0.7
5	(-54.0, 371.7, 1.0)	(-53.3, 371.5, 0.4)	-0.7	0.2	0.6
6	(-43.2, 342.2, 0.9)	(-44.3, 342.1, 0.1)	1.1	0.1	0.8
7	(-47.9, 310.4, 1.8)	(-47.0, 310.7, 3.1)	0.9	-0.3	-1.3
8	(-60.2, 283.5, 5.4)	(-59.6, 284.4, 7.2)	-0.6	-0.9	-1.8
9	(-76.2, 266.4, 6.6)	(-77.0, 267.1, 8.2)	0.8	-0.7	-1.6
10	(-96.7, 260.2, 6.3)	(-95.8, 259.4, 6.5)	-0.9	0.8	-0.2
11	(-113.8, 260.1, 6.4)	(-114.2, 259.6, 6.7)	0.4	0.5	-0.3
12	(-133.6, 267.7, 7.1)	(-132.3, 267.1, 8.8)	-1.3	0.6	-1.7
13	(-146.3, 280.9, 7.8)	(-147.9, 281.3, 8.6)	1.6	-0.4	-0.8
14	(-158.4, 297.4, 7.2)	(-158.2, 298.7, 6.0)	-0.2	-1.3	1.2
15	(-161.7, 327.4, 6.3)	(-162.4, 327.2, 5.0)	0.7	0.2	1.3

six-dimensional force sensor can detect the magnitude and direction of the constantly changing three-dimensional force and three-dimensional moment of force in real time. The force direction of the sensor is consistent with the pointing direction of the end-effector, that is, the normal direction of the breast surface. The collected force data are transmitted to the computer. The data are not constant but are constantly changing. A flexible force/position control strategy is used, and the position and posture of the ultrasonic probe are corrected in real time through the feedback information of the six-dimensional force sensor, so that the closed-loop feedback control is realized. Due to the fluidity of breast tissue, the breast model is easily disturbed in the scanning process, thus affecting the change of the actual path. Therefore, to reduce the error of the force feedback signal in the experiment, the fuzzy PD algorithm is used to reduce the magnitude of the dynamic deviation. Figure 23 is the structural block diagram of force feedback pose adjustment. In Figure 23, S and S' represent position control matrix parameters and force control matrix parameters, respectively. X is the position input value, ΔX is the position deviation value, and X_e is the expected pose of the final output. F_e is the expected contact force, F is the actual contact force, and ΔF is the contact force deviation value. θ_e is the expected joint angle.

Figure 22 is a comparison diagram of the theoretical path and the actual path. The experimental results in Table 4 show that there is little error between the actual motion effect and the theoretical motion effect. The errors of X, Y and Z axis are very small. However, Figure 21 shows that the error between the theoretical coordinates and actual coordinates in the z direction is greater than the errors in the x and y directions. In order to reach the maximum scanning range, the x-y plane is used as the projection plane, and the influence of the z coordinate is mainly considered in the process of 3D reconstruction and path planning. Through the calculation of experimental data, the average errors of the theoretical motion path and the actual motion path in XYZ directions are 0.79 mm, 0.49 mm and 0.89 mm, and the standard deviations are 0.90 mm, 0.58 mm and 1.04 mm. The actual results are basically consistent with the theoretical results. The robot can complete the breast ultrasonic scanning operation according to the preset path planning results.

VI. CONCLUSION AND FUTURE WORK

In this paper, we studied the scanning path planning of the robot for breast ultrasound examination and proposed a method for extracting breast ultrasonic scanning path based on binocular vision and NURBS. The binocular vision system is utilized to obtain the image information. The calibration and distortion correction are carried out for the binocular camera. The stereo matching process is defined. According to the matching cost, cost aggregation and parallax calculation, the 3D point cloud reconstruction of the breast model is completed. The scanning path extraction based on the breast point cloud model is accomplished, and the model is optimized. Then, the ultrasonic scanning path is interpolated and optimized according to the interpolation optimization ability of the NURBS curve. The smoothly fitted ultrasonic scanning path is set as the motion path of the robot. The experimental platform for breast ultrasound examination based on the UR5e robot was built to obtain the actual motion path and to carry out an error analysis experiment. Analysis of the experimental data suggests that the actual motion effect is consistent with the theoretical motion effect. The average

errors of the actual motion path and the planned motion path are 0.79 mm, 0.49 mm and 0.89 mm, and the standard deviations are 0.90 mm, 0.58 mm and 1.04 mm. The experiments verify the accuracy of the scanning path planning results of the robot.

This paper solves the path planning problem of breast ultrasound examination robots, and improves the automation and intelligence of breast ultrasound examination. Future work will focus on the following aspects.

1. The stereo matching method should be further optimized to improve the accuracy of image matching. According to breast feature points, we will develop a more adaptive matching method to solve the problem of stereo matching delay.

2. The force feedback device is added to the robot to improve the perception ability of the robot in breast ultrasound examination. This device can improve the safety of the operation and enhance the medical effect of breast ultrasound examination. We will further study the force control strategy in the future.

REFERENCES

[1] M. Ghoncheh, Z. Pournamdar, and H. Salehiniya, "Incidence and mortality and epidemiology of breast cancer in the world," *Asian-Pacific J. Cancer Prevention*, vol. 17, no. sup3, pp. 43–46, Jun. 2016.

[2] H. Sung, J. Ferlay, R. L. Siegel, M. Laversanne, I. Soerjomataram, A. Jemal, and F. Bray, "Global cancer statistics 2020: GLOBOCAN estimates of incidence and mortality worldwide for 36 cancers in 185 countries," *CA, A Cancer J. Clinicians*, vol. 71, no. 3, pp. 209–249, May 2021.

[3] A. Ahmad, "Breast cancer statistics: Recent trends," in *Breast Cancer Metastasis Drug Resistance* (Advances in Experimental Medicine and Biology), vol. 1, 2nd ed. Cham, Switzerland: Springer, 2019, pp. 1–7.

[4] O. Ginsburg, C. H. Yip, A. Brooks, A. Cabanes, M. Caleffi, J. A. D. Yataco, B. Gyawali, V. McCormack, M. M. De Anderson, R. Mehrotra, and A. Mohar, "Breast cancer early detection: A phased approach to implementation," *Cancer*, vol. 126, pp. 2379–2393, May 2020.

[5] J. Zheng, D. Lin, Z. Gao, S. Wang, M. He, and J. Fan, "Deep learning assisted efficient AdaBoost algorithm for breast cancer detection and early diagnosis," *IEEE Access*, vol. 8, pp. 96946–96954, 2020.

[6] R. F. Brem, M. J. Lenihan, J. Lieberman, and J. Torrente, "Screening breast ultrasound: Past, present, and future," *Amer. J. Roentgenol.*, vol. 204, no. 2, pp. 234–240, Nov. 2015.

[7] B. J. Burkett and C. W. Hanemann, "A review of supplemental screening ultrasound for breast cancer: Certain populations of women with dense breast tissue may benefit," *Acad. Radiol.*, vol. 23, no. 12, pp. 1604–1609, 2016.

[8] U. R. Acharya, K. M. Meiburger, J. E. W. Koh, E. J. Ciaccio, N. Arunkumar, M. H. See, N. A. M. Taib, A. Vijayananthan, K. Rahmat, F. Fadzli, S. S. Leong, C. J. Westerhout, A. Chantre-Astaiza, and G. Ramirez-Gonzalez, "A novel algorithm for breast lesion detection using textons and local configuration pattern features with ultrasound imagery," *IEEE Access*, vol. 7, pp. 22829–22842, 2019.

[9] L. De Raeymaekers, N. M. Illemann, T. J. Als, M. G. Skjødt, M. S. Tvergaard, and L. N. S. A. Struijk, "Preliminary examination of the potential of robot-assisted sonography—An ergonomic tool for obstetric sonographers," *Appl. Ergonom.*, vol. 96, Oct. 2021, Art. no. 103479.

[10] M. Lu, Y. Zhang, and H. Du, "Design and control of a novel magnetic resonance imaging-compatible breast intervention robot," *Int. J. Adv. Robotic Syst.*, vol. 17, no. 3, May 2020, Art. no. 172988142092785.

[11] X. Jia, Y. Zhang, J. Jiang, H. Du, and Y. Yu, "Design and analysis of a novel long-distance double tendon-sheath transmission device for breast intervention robots under MRI field," *Adv. Mech. Eng.*, vol. 12, no. 3, Mar. 2020, Art. no. 168781402090456.

[12] F. Suligoj, C. M. Heunis, J. Sikorski, and S. Misra, "RobUSt—An autonomous robotic ultrasound system for medical imaging," *IEEE Access*, vol. 9, pp. 67456–67465, 2021.

[13] Y. Han, K. Zhao, Z. Chu, and Y. Zhou, "Grasping control method of manipulator based on binocular vision combining target detection and trajectory planning," *IEEE Access*, vol. 7, pp. 167973–167981, 2019.

[14] S. Lu, B. Ding, and Y. Li, "Minimum-jerk trajectory planning pertaining to a translational 3-degree-of-freedom parallel manipulator through piecewise quintic polynomials interpolation," *Adv. Mech. Eng.*, vol. 12, no. 3, Mar. 2020, Art. no. 168781402091366.

[15] S. Lu, Y. Li, and B. Ding, "Kinematics and dynamics analysis of the 3PUS-PRU parallel mechanism module designed for a novel 6-DOF gantry hybrid machine tool," *J. Mech. Sci. Technol.*, vol. 34, no. 1, pp. 345–357, Jan. 2020.

[16] A. AbbasiMoshaii and F. Najafi, "Design, evaluation and prototyping of a new robotic mechanism for ultrasound imaging," *J. Comput. Appl. Mech.*, vol. 50, no. 1, pp. 108–117, 2019.

[17] R. Monfaredi, E. Wilson, B. A. Koutenaei, B. Labrecque, K. Leroy, J. Goldie, E. Louis, D. Swerdlow, and K. Cleary, "Robot-assisted ultrasound imaging: Overview and development of a parallel telerobotic system," *Minimally Invasive Therapy Allied Technol.*, vol. 24, no. 1, pp. 54–62, 2015.

[18] J. Sandoval, M. A. Laribi, S. Zeghloul, M. Arsicault, and J.-M. Guilhem, "Cobot with prismatic compliant joint intended for Doppler sonography," *Robotics*, vol. 9, no. 1, p. 14, Mar. 2020.

[19] R. Kojcev, A. Khakzar, B. Fuerst, O. Zettinig, C. Fahkry, R. DeJong, J. Richmon, R. Taylor, E. Sinibaldi, and N. Navab, "On the reproducibility of expert-operated and robotic ultrasound acquisitions," *Int. J. Comput. Assist. Radiol. Surgery*, vol. 12, no. 6, pp. 1003–1011, Jun. 2017.

[20] M. Giuliani, D. Szczęśniak-Staáczyk, N. Mirnig, G. Stollnberger, M. Szyszko, B. Staáczyk, and M. Tscheligi, "User-centred design and evaluation of a tele-operated echocardiography robot," *Health Technol.*, vol. 10, no. 3, pp. 649–665, May 2020.

[21] T. Xu and Y. Xia, "Guidance for acupuncture robot with potentially utilizing medical robotic technologies," *Evid-Based Complement Alternative Med.*, vol. 2021, p. 11, Mar. 2021.

[22] Y. Lin, Y. Shi, F. Wang, J. Zhang, H. Sun, and W. Wu, "Development and placement accuracy evaluation of an MR conditional robot for prostate intervention," *Med. Biol. Eng. Comput.*, vol. 59, no. 5, pp. 1023–1034, May 2021.

[23] L. Zhang, C. Li, Y. Fan, X. Zhang, and J. Zhao, "Physician-friendly tool center point calibration method for robot-assisted puncture surgery," *Sensors*, vol. 21, no. 2, p. 366, Jan. 2021.

[24] K. Xu, Z. Chen, and F. Jia, "Unsupervised binocular depth prediction network for laparoscopic surgery," *Comput. Assist. Surg.*, vol. 24, no. sup1, pp. 30–35, 2019.

[25] R. Wang, Y. Han, M. Z. Luo, N. K. Wang, W. W. Sun, S. C. Wang, H. D. Zhang, and L. J. Lu, "Accuracy study of a binocular-stereo-vision-based navigation robot for minimally invasive interventional procedures," *World J. Clin. Cases*, vol. 8, no. 16, p. 3440, 2020.

[26] G. Jiang, M. Luo, and K. Bai, "Optical positioning technology of an assisted puncture robot based on binocular vision," *Int. J. Imag. Syst. Technol.*, vol. 29, no. 2, pp. 180–190, 2019.

[27] J. Jahanpour, M. Motallebi, and M. Porghoveh, "A novel trajectory planning scheme for parallel machining robots enhanced with NURBS curves," *J. Intell. Robotic Syst.*, vol. 82, no. 2, pp. 257–275, May 2016.

[28] A. Hashemian, S. F. Hosseini, and S. N. Nabavi, "Kinematically smoothing trajectories by NURBS reparameterization—An innovative approach," *Adv. Robot.*, vol. 31, nos. 23–24, pp. 1296–1312, Dec. 2017.

[29] G. Wu, W. Zhao, and X. Zhang, "Optimum time-energy-jerk trajectory planning for serial robotic manipulators by reparameterized quintic NURBS curves," *Proc. Inst. Mech. Eng., C, J. Mech. Eng. Sci.*, vol. 235, no. 19, Oct. 2021, Art. no. 0954406220969734.

[30] M. She and L. Tian, "A novel path control algorithm for networked underwater robot," *J. Robot.*, vol. 2018, pp. 1–7, Jul. 2018.

[31] F. Gu, H. Zhao, Y. Ma, and P. Bu, "Camera calibration based on the back projection process," *Meas. Sci. Technol.*, vol. 26, no. 12, Dec. 2015, Art. no. 125004.

[32] M. Shao, P. Wang, and Y. Wang, "Phase-based calibration method for a binocular vision sensor," *IEEE Access*, vol. 9, pp. 44354–44362, 2021.

[33] T. Xu, D. An, Z. Wang, S. Jiang, C. Meng, Y. Zhang, Q. Wang, Z. Pan, and Y. Yue, "3D joints estimation of the human body in single-frame point cloud," *IEEE Access*, vol. 8, pp. 178900–178908, 2020.

[34] A. Ravankar, A. A. Ravankar, Y. Kobayashi, Y. Hoshino, and C.-C. Peng, "Path smoothing techniques in robot navigation: State-of-the-art, current and future challenges," *Sensors*, vol. 18, no. 9, p. 3170, Sep. 2018.

[35] S. Jalel, P. Marthon, and A. Hamouda, "A new path generation algorithm based on accurate NURBS curves," *Int. J. Adv. Robotic Syst.*, vol. 13, no. 2, p. 75, Mar. 2016.

XINRAN ZHANG was born in Heilongjiang, China, in 1996. She received the B.Sc. degree in mechatronic engineering from the Harbin University of Science and Technology, Harbin, Heilongjiang, in 2015, where she is currently pursuing the Ph.D. degree in mechatronic engineering.

Her research interests include breast particle implantation robot, minimally invasive interventional robots, and brachytherapy robots.

YONGDE ZHANG (Member, IEEE) was born in Jilin, China, in 1965. He received the B.S. degree in mechanical engineering and the M.S. degree and the Ph.D. degree in mechanical engineering from the Harbin Institute of Technology, Harbin, Heilongjiang, China, in 1988, 1993, and 1999, respectively.

From 1999 to 2001, he worked as an Associate Researcher with the Automation Research Center, City University of Hong Kong. In 2004, he worked as a Researcher with the Computer-Assisted Interventional Medicine Laboratory, Nanyang Technological University, Singapore. From 2004 to 2006, he was a Visiting Scholar with the University of Rochester Medical Center. Since 2007, he has been a Professor and a Doctoral Supervisor with the School of Mechanical Power Engineering and Robotics and the Engineering Research Center, Harbin University of Science and Technology. His current research interests include medical robots, education robots, and biomimetic.

HAIYAN DU was born in Liaoning, China, in 1975. She received the B.Sc. degree in mechatronic engineering from the Harbin University of Science and Technology, in 1999, the M.S. degree from the Harbin Institute of Technology, in 2004, and the Ph.D. degree in mechanical manufacturing and automation from the Harbin University of Science and Technology, in 2015.

She is currently an Associate Professor and a Master Supervisor with the Harbin University of Science and Technology. Her current research interests include medical robot, educational robot, and electromechanical system control.

MINGYUE LU was born in Heilongjiang, China, in 1993. She received the B.Sc. degree from Dalian Polytechnic University, in 2016. She is currently pursuing the Ph.D. degree in mechatronic engineering with the Harbin University of Science and Technology.

Her research interests include breast intervention robot, minimally invasive interventional robots, and brachytherapy robots.

ZIXI ZHAO was born in Heilongjiang, China, in 1995. She received the B.Sc. and M.Sc. degrees in mechatronic engineering from the Harbin University of Science and Technology, in 2018 and 2020, respectively.

Her research interests include breast interventional robot, ultrasonography, and three-dimensional reconstruction of breast.

YANHUA ZHANG was born in Heilongjiang, China, in 1962. She received the B.Sc. degree and the M.S. degree in imaging medicine and nuclear medicine from Harbin Medical University, Harbin, Heilongjiang, in 1985 and 2001, respectively.

She is currently a Chief Physician and an Associate Professor with Harbin Medical University Cancer Hospital. Her research interests include interventional ultrasound diagnosis of abdominal, small organ, and urinary tumors.

SIHAO ZUO was born in Heilongjiang, China, in 1992. He received the B.Sc. and M.Sc. degrees in mechatronic engineering from the Harbin University of Science and Technology, in 2014 and 2018, respectively, where he is currently pursuing the Ph.D. degree in mechatronic engineering.

His research interests include medical robots, minimally invasive interventional robots, and particle implantation robot.